Stable and Unstable Lipid Domains in Ceramide-Containing Membranes

Beate Boulgaropoulos,[†] Zoran Arsov,[‡] Peter Laggner,[†] and Georg Pabst[†]*
[†]Institute of Biophysics and Nanosystems Research, Austrian Academy of Sciences, Graz, Austria; and [‡]Laboratory of Biophysics, Jozef Stefan Institute, Ljubljana, Slovenia

ABSTRACT We applied x-ray diffraction, calorimetry, and infrared spectroscopy to lipid mixtures of palmitoyl-oleoyl phosphatidylcholine, sphingomyelin, and ceramide. This combination of experimental techniques allowed us to probe the stability and structural properties of coexisting lipid domains without resorting to any molecular probes. In particular, we found unstable microscopic domains (compositional/phase fluctuations) in the absence of ceramide, and macroscopically separated fluid and gel phases upon addition of ceramide. We also observed phase fluctuations in the presence of ceramide within the broad phase transition regions. We compare our results with fluorescence spectroscopy data and complement the previously reported phase diagram. We also obtained electron paramagnetic resonance data to assess the possible limitations of techniques employing a single label. Our study demonstrates the necessity of applying a combination of experimental techniques to probe local/global structural and fast/slow motional properties in complex lipid mixtures.

INTRODUCTION

Biological membranes are generally considered to be a highly dynamic material with structural domains (e.g., rafts) that are crucial for several cellular functions (1–3). Lipid domains are also observed in well-defined mixtures of membrane lipids, and several biophysical techniques have been developed with the aim to determine the phase diagrams of membrane lipid mixtures and gain insight into the nature of membrane rafts (4–7). However, the phase diagrams reported to date are often controversial with respect to the form of the phase coexistence region (closed loop versus open loop) or direction of the tie lines (7). Major sources of confusion are the inherent timescales and length scales of the applied techniques. Microscopy or elastic diffraction techniques, for example, report on the global structural properties of membranes in the range of seconds to minutes (4,8). Spectroscopic techniques are sensitive in the nanosecond–millisecond time regime and report on very localized environments (7). Considering these aspects in relation to the structural heterogeneity of membranes, which may originate from either small, unstable domains (compositional/phase fluctuations, nonideal/nonrandom mixing, microscopic phase separation) or large micron-sized, stable domains (macroscopic phase separation) (8), the discrepancies among reported phase diagrams are not surprising. Whereas spectroscopic techniques can detect compositional fluctuations, global techniques are ideally suited to detect macroscopic phase separation (8). Additional complications may arise because of the possible influence of fluorescence labels on phase equilibria (9–12).

To address these issues, we combined three label-free experimental techniques: small- and wide-angle x-ray scattering (SWAXS), attenuated total reflection Fourier transform infrared spectroscopy (ATR-FTIR), and differential scanning calorimetry (DSC). SWAXS provides information on the overall membrane structure from positional correlations of the bilayers and hydrocarbon chains (8), and thus provides a global picture of stable macroscopic lipid domains. In general, DSC probes the thermotropic properties of a system, but the form of the transition peaks (e.g., their width) also contains information on the lipid mixing (stable and unstable domains) behavior (13). IR spectroscopy provides information on the level of local lipid ordering (14) and on intermolecular interactions (e.g., hydrogen bonding) (15) with an inherent timescale in the subnanosecond regime. Therefore, it is suitable for studying dynamic microscopic domains, in particular because lateral diffusion of lipids and domain lifetime cannot cause averaging of the spectroscopic properties across different domains (16). In this study, our goal was to demonstrate the ability of this combination of tools to differentiate between microscopic (unstable) and macroscopic (stable) phase separation in a lipid model system in the absence of probes. In addition, we performed electron paramagnetic spectroscopy (EPR) using a fatty acid spin label to address possible discrepancies with a labeling technique.

We focused on a particular ternary lipid mixture of palmitoyl-oleoyl phosphatidylcholine (POPC), sphingomyelin (SM), and ceramide (Cer). This system is of biological interest because SM may be enzymatically hydrolyzed by sphingomyelinase (e.g., during apoptosis) to Cer, which may act as a second messenger or influence cellular activities by modulating the biophysical properties of the membrane (17–19). For example, Cer induces the formation of Cer-enriched gel-like domains (20) and thus is believed to stabilize membrane rafts (19,21). Recently, we were able to show that the biological activity of sphingomyelinase is strictly controlled by the evolving SM/Cer molar ratio

Submitted November 10, 2010, and accepted for publication March 15, 2011.

*Correspondence: georg.pabst@oeaw.ac.at

Editor: Thomas J. McIntosh.

0006-3495/11/05/2160/9 $2.00

doi: 10.1016/j.bpj.2011.03.013

(22). It is therefore of interest to determine the Cer concentration regimes in which the lateral membrane structure will exhibit microscopic or macroscopic demixing. In particular, we characterized a cut through the POPC/SM/Cer phase diagram along the SM + Cer = 50 mol % line of egg-SM and C16:0 Cer. We discuss our findings in comparison with previous results obtained from a similar lipid mixture by fluorescence labeling techniques (23).

MATERIALS AND METHODS

Lipids

POPC (1-palmitoyl-2-oleoyl-*sn*-glycero-3-phosphocholine), egg-SM ((2S,3R,4E)-2-acylaminooctadec-4-ene-3-hydroxy-1-phosphocholine), and C16:0-Cer ((2S,3R,4E)-2-palmitoylaminooctadec-4-ene-1,3-diol) were purchased from Avanti Polar Lipids (Birmingham, AL) and used without further purification. All other chemicals were obtained from Sigma-Aldrich (St. Louis, MO) and were of professional analysis quality.

Preparation of liposomes

Lipid stock solutions were prepared by dissolving weighted amounts of dry lipid powder in chloroform/methanol (2:1, v/v). After the appropriate volumes of the stock solutions were mixed, the organic solvent was evaporated at room temperature under a gentle stream of nitrogen. The vials were then placed under vacuum for at least 12 h to remove all traces of the organic solvent. The resulting dry lipid films were suspended for x-ray and DSC experiments in 20 mM Na-phosphate buffer (130 mM NaCl, pH = 7.4). For IR experiments, the films were hydrated with 18 MΩ/cm water. All samples were incubated for 4 h in the fluid phase and intermittently vigorously vortex-mixed. At least eight freeze-thaw cycles were applied with the use of liquid nitrogen.

DSC measurements

DSC measurements were performed on a VP-DSC high-sensitivity differential scanning calorimeter (MicroCal, Northampton, MA). The lipid concentration was 1 mg/ml for the equimolar POPC/SM mixture. Samples containing Cer showed a transition that approached 0°C with increasing Cer concentration and were measured in an extended temperature range, i.e., with the scan initiated at −7°C. To avoid freezing of the DSC cell, these samples were contained in stainless-steel capillaries filled with 10 μl of the lipid dispersion (concentration 200 mg/ml) and sealed with nylon plugs. The capillaries were inserted into the calorimeter cell containers, which were filled with glycerol solution. Each DSC experiment consisted of three heating and three cooling scans. Samples were tempered for 30 min before each heating and cooling scan, respectively. The scan rate for all experiments was 0.5°C/min. Origin software (MicroCal) was used for data acquisition, baseline adjustment, normalization by the lipid concentration, and analysis throughout. The phase-transition temperatures were derived from the temperatures at the peak maximum of heat capacity (c_P). The on- and off-temperatures, T_{on}/T_{off}, were determined by means of the tangent method as the intersection of the peak slopes with the baseline of the thermograms (24).

SWAXS experiments

SWAXS experiments were performed on a SWAXS camera (System 3, Hecus X-Ray Systems, Graz, Austria). The x-ray camera was mounted on a sealed-tube generator (GE-Seifert, Ahrensburg, Germany) operating at 2 kW. CuK$_\alpha$ radiation ($\lambda = 1.542$ Å) was selected with the use of a Ni filter in combination with a pulse height discriminator. The x-ray beam size was set to 0.5 mm × 35 mm (V × H). The SWAXS patterns were recorded using two linear, one-dimensional, position-sensitive detectors (PSD 50; Hecus X-Ray Systems) for wave vectors ($q = 4\pi \sin\theta/\lambda$) 10^{-3} Å^{-1} < q < 1 Å^{-1} (SAXS) and 1.2 Å^{-1} < q < 2.7 Å^{-1} (WAXS). The samples were put into thin-walled, quartz-glass capillaries (1 mm diameter) in good thermal contact with a programmable Peltier unit and equilibrated for 10 min at each temperature before measurements were obtained. The exposure times were 3000 s.

Calibration was performed with para bromo-benzoic acid in the wide-angle region (25) and with silver-stearate in the small-angle region (d = 48.68 Å). The lamellar repeat distances were derived from the SAXS peak positions. From the Lorentz fits to the WAXS peaks, we took the peak center (q_{11}) to calculate the lateral area per lipid chain: $A_c = 8\pi^2/(\sqrt{3}\cdot q_{11}^2)$. The lateral correlation length (domain size) was estimated from $L = 2\pi/\sqrt{\Delta q_{corr}}$, where Δq_{corr} is the full width at half-maximum of the wide-angle gel peak corrected for the width of the vertical beam profile. The total lipid concentration for the x-ray diffraction experiments was 50 mg/ml.

ATR-FTIR spectroscopy

ATR-FTIR spectra were recorded on a Vertex 70 infrared spectrometer (Bruker Optics, Ettlingen, Germany) equipped with a liquid-nitrogen-cooled mercury-cadmium telluride detector and fitted with a Horizon ATR unit (Harrick Scientific, Pleasantville, NY). The internal reflection element (IRE) was a trapezoidal germanium ATR plate (50 × 10 × 2 mm) with an incidence angle of 45° yielding 25 internal reflections (New Era Enterprises, Vineland, NJ). Sixteen scans were averaged for each spectrum. The spectra were recorded at a nominal resolution of 2 cm^{-1}. The spectrometer and the ATR unit were continuously purged with dry nitrogen gas. The holder for the IRE was placed in tight contact with an aluminum block and the temperature was controlled by a circulating water bath connected to the sample mount. Then 200 μl of the liposome suspension (20 mg/ml) were spread over the germanium IRE. After the water evaporated, the dried lipid stacks were rehydrated with 300 μl D_2O and incubated above the melting transition. This ensured a complete hydrogen-deuterium exchange, as verified by the complete disappearance of the amide II band. To accentuate this, we denote the amide I band observed in the absorption spectra as the amide I′ band. We analyzed the ATR-FTIR spectra using the OPUS software package (version 5.5; Bruker Optics). To examine a particular region of the ATR-FTIR, we cut the spectra to an appropriate frequency range and subsequently baseline-corrected them with a straight line.

With regard to the analysis presented here, it is important to note that the carbonyl band relates to the properties of the phosphatidylcholines (PCs) at the lipid-water interface (in this case, POPC). In turn, the amide band reports on the sphingolipid-water interface (i.e., SM and Cer). Both bands overlapped only very weakly, facilitating our analysis of POPC's properties at the water-lipid interface separately from those of SM/Cer. In previous studies, Arsov and Quaroni (26,27) used curve-fitting to show that the carbonyl and amide I′ bands of particular lipids are composed of two major components representing the populations of hydrogen-bonded and nonhydrogen-bonded lipids. In the case of PCs, hydrogen bonds are formed with water, whereas in the case of SM, hydrogen bonds can also form between neighboring SM molecules (27). Typically, resolution enhancement by Fourier self-deconvolution and second-derivative calculation provides values of the peak positions of particular components, whereas amplitudes and widths are determined by fitting. In this study, the fitted region of the ATR-FTIR spectra extended over both the amide I′ and carbonyl bands (see Fig. S3 in the Supporting Material). A detailed description of the curve-fitting procedure used is given elsewhere (26,27).

EPR spectroscopy

The lipophilic spin probe MeFASL (10,3), which is the methyl ester of 5-doxyl palmitate (synthesized by S. Pečar, Faculty of Pharmacy,

University of Ljubljana, Ljubljana, Slovenia) was dissolved in ethanol at a concentration of 0.1 mM. Then 50 μl of this solution were transferred to a plastic tube, evaporated, and subsequently mixed with 100 μl of the prepared liposomal dispersions. The tube was then rotated for 10 min at 65°C and subsequently vortex-mixed for 5 min. Finally, the sample was transferred to a quartz-glass capillary (1 mm inner diameter) for measurements. EPR spectra were recorded on an Elexsys E500 spectrometer (Bruker, Karlsruhe, Germany) with a 9.34 GHz microwave frequency, 20 mW power, 100 kHz modulation frequency, and 0.1 mT amplitude. The ratio of the number of spin probe molecules to the number of lipid molecules was ~1/500.

RESULTS AND DISCUSSION

All experiments were repeated at least twice to ensure repeatability. Furthermore, experiments were performed at various times after sample hydration, ranging from hours to several days or weeks. We did not observe any significant differences in the reported parameters. Therefore, we can exclude possible influences from the kinetics of domain formation reported previously for different ternary lipid mixtures (12,28). Unless stated otherwise, the reported errors originate from uncertainties in determining the peak positions and intersecting lines.

Thermotropic behavior

Our first insight into the POPC/SM/Cer mixtures was obtained by DSC. Pure POPC exhibited a melting transition at −3.3°C, in agreement with previous results (29), and egg-SM showed a narrow transition at 39.2°C, which also agrees with literature data (30,31). Finally, the transition temperature of C16:0 Cer was reported to occur at 90.0°C (32). To mimic the enzymatic generation of Cer in an equimolar mixture of POPC and SM, we systematically replaced SM by Cer, keeping the total molar ratio of POPC/(SM + Cer) = 1 constant. This corresponds to a cut in the ternary phase diagram of the system along the line of SM + Cer = 50 mol %.

The binary POPC/SM mixture showed a single broad main transition at T_m = 21.3°C with a halfwidth of ~8°C, indicating a low cooperativity of the transition (Fig. 1). Broadening could be also caused by a convolution of several melting components; however, this is beyond our present resolution. The transition temperature and range are in agreement with previous DSC measurements (30) and fluorescence spectroscopy results from POPC/C16:0-SM (33). In the presence of 5 mol % Cer, the single transition peak split into two broad peaks. The first transition occurred at slightly lower temperatures (T_{m1} = 19°C), and the second transition shifted significantly to higher temperatures (T_{m2} = 44°C). With a further increase in Cer concentration, the two transition peaks separated on the temperature axis. Thus, one peak approached the T_m of pure POPC, and the second peak shifted more and more toward higher temperatures, away from the T_m of pure SM (Table 1). The widths of the transition regimes, however, did not change significantly

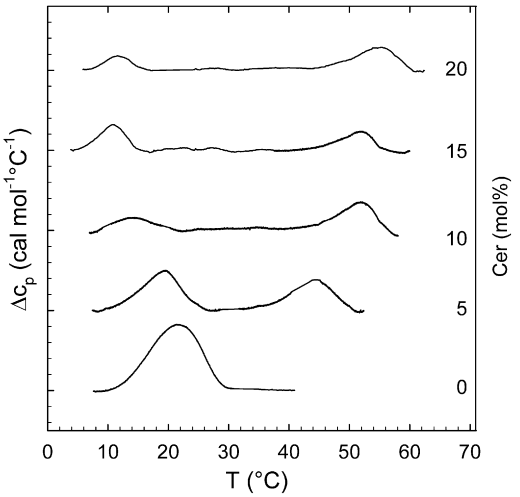

FIGURE 1 Thermograms of second DSC heating scans for various POPC/SM/Cer mixtures. Curves were shifted vertically for better graphic representation. Numbers to the right denote Cer concentration in mol %.

as a function of Cer concentration. Due to uncertainties in the baseline subtraction (i.e., low peak heat capacities and nonmonotonic behavior of the baseline), we refrained from evaluating the transition enthalpies. DSC scans of membranes containing 35 mol % were significantly different and showed an exothermal peak at 64°C and an endothermal transition at 90°C (Fig. S1). This agrees with thermodynamic data reported for C16:0 Cer (32) and suggests the formation of pure Cer domains, as discussed below.

Structural characterization of the coexistence region

As a next step, we focused on the structural features of the membranes in the region between T_{m1} and T_{m2} using SWAXS. We previously showed that this regime corresponds to a macroscopic phase coexistence of gel L_β and fluid L_α phases (20). To emphasize that these domains are stable, we denote them in the following text as L_β(s) and L_α(s). We now describe their behavior as a function of temperature and Cer concentration in more detail.

The wide-angle data (Fig. 2) show the packing of the hydrocarbon chains. A WAXS peak occurs, for example, for the 15 mol % Cer sample (T = 37°C) at q = 1.52 Å^{-1} and is characteristic for a hexagonal packing of untilted hydrocarbon chains of the L_β(s) phase. The L_α(s) phase shows a broad WAXS peak at q ~1.4 Å^{-1} (20). However, because this is too diffuse to be observed in our experiments, our description of the WAXS data is focused on the L_β(s) chain packing. As the temperature and the Cer concentration were varied, the corresponding WAXS peak shifted its position and also changed in width (see Fig. 2 *A* for the 15 mol % Cer sample). No clear WAXS peak was observed in the patterns from 5°C to 15°C, coinciding with the broad T_{m1}

TABLE 1 Thermotropic data for POPC/SM/Cer mixtures as derived from DSC and ATR-FTIR data (in parentheses)

Sample	Cer (mol %)	T_{m1} (°C)	T_{on}/T_{off1} (°C)	T_{m2} (°C)	T_{on}/T_{off2} (°C)
POPC	0	−3.3 ± 0.5	−3.6/−2.1 ± 0.5		
SM	0	39.0 ± 0.5	35.9/40.0 ± 0.5		
POPC/SM/Cer	0	21 ± 1	12/29 ± 1 (16/33 ± 2)		
	5	19 ± 2	11/25 ± 2 (–/24 ± 2)	44 ± 2	37/51 ± 2 (–/54 ± 2)
	10	15 ± 2	7/22 ± 2	51 ± 2	44/56 ± 2
	15	11 ± 2	5/15 ± 2 (–)	51 ± 2	44/56 ± 2 (41/61 ± 2)
	20	12 ± 2	7/16 ± 2 (–)	54 ± 2	46/60 ± 2 (39/63 ± 2)

The "(–)" denotes instances in which the IR data could not be evaluated because T_{on}/T_{off} was outside the studied temperature interval, or the change in slope of the symmetric CH_2 band was not significant.

phase transition regime (Table 1) and indicating a loose lipid packing in this regime. Between 20°C and 60°C, the WAXS peaks shifted to smaller q-values, indicating an increase of the lateral distance between the acyl chains. Finally, the WAXS peak was absent at 70°C, in agreement with the melting of $L_\beta(s)$ at T_{m2} (Fig. 1). Fig. 2 *B* shows the formation of the WAXS peak as a function of Cer concentration at 37°C. According to the DSC data, in the absence of Cer the system is in the fluid phase at this temperature and therefore shows no WAXS peak (Fig. 1). A clear signal of a gel peak was present below the T_m, however (Fig. S2). With increasing Cer concentration, the WAXS peak at 37°C became more pronounced, indicating a progressive formation of the $L_\beta(s)$ phase.

To gain more quantitative insight, we analyzed the WAXS data in terms of the lateral area per acyl chain A_C and the lateral domain size L as described in the previous section. The area per lipid chain within the gel domains generally increased upon heating and upon Cer addition (Fig. 3 *A*). This signifies a lateral expansion of the membrane upon

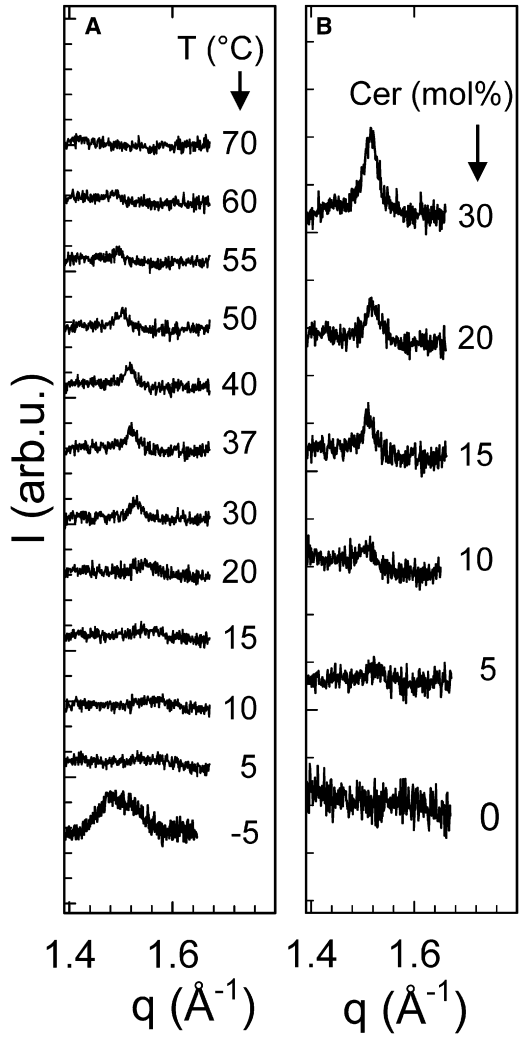

FIGURE 2 WAXS patterns of POPC/SM/Cer mixtures as a function of temperature (*A*: 15 mol % Cer) and Cer concentration (*B*: T = 37°C). Temperatures and Cer content (mol %) are given on the right.

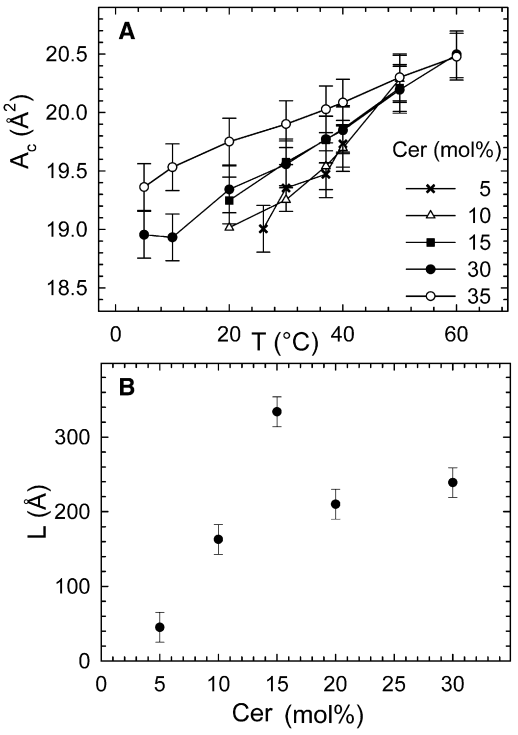

FIGURE 3 Packing properties of the $L_\beta(s)$ phase. (*A*) Temperature dependence of the lateral area per acyl chain. (*B*) Dependence of the lateral correlation length (domain size) on Cer concentration at 37°C.

heating and Cer addition. However, $\Delta A_C/\Delta T$ decreased upon Cer addition, which suggests a stabilization of the $L_\beta(s)$ phase with increasing Cer content. The average lateral domain size, L, as determined from the peak width, in turn showed a nonmonotonic behavior as a function of Cer concentration (Fig. 3 *B*). In particular, at 37°C, L exhibited a maximum size of ~340 Å at 15 mol % Cer, which is close to a SM/Cer molar ratio of 2. This indicates an optimal packing ratio for SM and Cer, and agrees with the coordination of 2–3 SM molecules per Cer suggested by fluorescence spectroscopy (34). However, more WAXS data close to 15 mol % Cer would be needed to support this notion.

We now present SAXS data relating to the supramolecular packing of the POPC/SM/Cer mixtures. We previously showed that the lamellar repeat distances of the $L_\alpha(s)$ and $L_\beta(s)$ phases are too similar to distinguish individual Bragg reflections in fully hydrated systems (20,22). The ribbon-shaped x-ray beam used in the experiments presented here added instrumental smearing to the data, which makes it even more difficult to differentiate the coexisting phases. We observed a broadening of the Bragg reflections due to the nearly overlapping peaks of the $L_\alpha(s)/L_\beta(s)$ phases. Application of osmotic pressure would resolve this problem. However, since we previously demonstrated the existence of the $L_\alpha(s)$ and $L_\beta(s)$ phases under the same conditions used here (20,22), it is sufficient to study the fully hydrated systems as a function of temperature and Cer content. Thus, it is important to keep in mind that the single repeat distance, d, we report from the data is a convolution of the d-values of the $L_\alpha(s)$ and $L_\beta(s)$ phases. However, because the d-value of the $L_\beta(s)$ phase is slightly larger than that of the $L_\alpha(s)$ phase (20), our results will be dominated by the properties of the gel phase.

We start the description of the SAXS data with the binary POPC/SM mixture, which exhibits no macroscopic phase separation (20), also in agreement with earlier work (30). Of interest, gel-fluid phase coexistence was previously observed in POPC/C16:0 SM (35), indicating an influence of the distribution of hydrocarbon chains in egg-SM. We found that the lamellar repeat distance decreased monotonically with temperature from ~72 Å at 5°C in the gel phase to ~62.0 Å at 70°C in the fluid phase (Fig. 4 *A*). The largest drop in d occurred in the main transition regime. For the mixtures containing Cer, d decreased only a little in the $L_\alpha(s)/L_\beta(s)$ coexistence regime. Further, d decreased only slightly across T_{m2}. We observed, however, a significant general increase of d with Cer content, as shown in Fig. 4 *B* for T = 37°C. This behavior reflects the growth and stabilization of the $L_\beta(s)$ domains. Above 30 mol % Cer, the system entered into a new regime. As reported previously (22), the SAXS pattern of the 35 mol % Cer sample exhibited an additional peak at $d = 43.6$ Å. This peak originates from a pure Cer domain, which we denote as L_{Cer}. Note that precipitation of pure Cer was also observed by DSC (Fig. S1) and agrees with previous results (36).

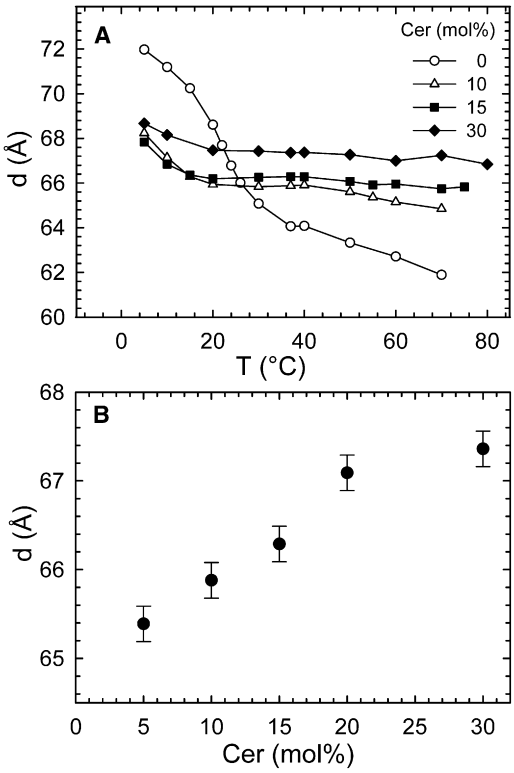

FIGURE 4 Lamellar lattice changes of the POPC/SM/Cer mixtures. (*A*) Temperature behavior (errors indicated by the size of the symbols). (*B*) Change in the lamellar repeat distance upon Cer addition at 37°C.

Vibrational dynamics

We focused on three vibrational bands: the symmetric methylene stretching band and the amide I′ (C=O stretching, C–N–H in-plane bending, C–N stretching) and carbonyl (C=O stretching) bands. The symmetric CH_2 band provides information on the conformational properties of acyl chains (14,37). We do not discuss the antisymmetric methylene stretching band, because it showed behavior similar to that of the symmetric band and contains overlaps with other vibrational modes (37). For all samples we observed a monotonic increase of vibrational frequency, ν_{CH2}, with temperature (Fig. 5 *A* and Fig. S4). At low temperatures, ν_{CH2} was typical for a gel phase. At high temperatures, ν_{CH2} was characteristic for a fluid phase. We first focus on the equimolar POPC/SM mixture (Fig. 5 *A*). In going from the gel to the fluid phase, ν_{CH2} increased in a sigmoidal fashion, rather than in a step-like manner. Further, T_{on} and T_{off} (deduced as shown in Fig. 5 *A*) signify a broad transition range, in agreement with DSC data (Table 1). This indicates phase coexistence. These observations and the fact that the x-ray data did not show any phase coexistence for POPC/SM (20) further suggest that the coexisting phases are not stable against thermal fluctuations. To emphasize that these domains are unstable, we denote them in the following as $L_\beta(u)$ and $L_\alpha(u)$.

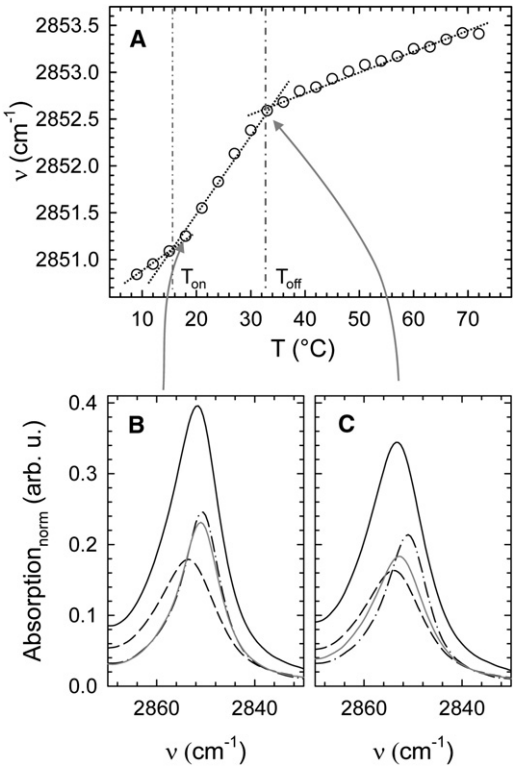

FIGURE 5 Symmetric CH_2 stretching band of POPC/SM (1/1). (*A*) Temperature dependence of the average peak position. Errors are ± 0.2 cm^{-1}. T_{on} and T_{off} are determined from the intercept of the slopes as indicated in the plot. (*B* and *C*) Comparison of the band region at 18°C (*B*) and 33°C (*C*). Dashed and dashed dotted lines show the bands of pure POPC and SM, respectively. The gray line corresponds to the calculated absorption band (see text). Absorption bands were normalized to the same area.

If the POPC and SM mixture exhibits a coexistence of L_β(u) and L_α(u), we should be able to decompose the symmetric CH_2 stretching band into its fluid-like (i.e., POPC-rich) and gel-like (i.e., SM-rich) components. Fig. 5, *B* and *C*, show the corresponding data at 18°C (i.e., in the POPC/SM main transition regime) and 33°C (i.e., at ~T_{off}; Table 1), respectively, in comparison with the spectra of pure POPC and SM. At 18°C, the POPC/SM band was centered at ν_{CH2}= 2851.3 cm^{-1}, whereas the pure POPC band occurred at ν_{CH2} = 2853.3 cm^{-1} and the pure SM band occurred at ν_{CH2} = 2850.5 cm^{-1}. We calculated the gray lines by subtracting half of the pure POPC band from the POPC/SM band, and obtained an almost perfect agreement with the pure SM band data at 18°C. The calculated SM CH_2 absorption data differed significantly from experimental data obtained at 33°C. This supports the notion that L_β(u) and L_α(u) form in the transition regime, and POPC and SM seem to mix well toward T_{off}.

Further support for this idea is obtained from the carbonyl and amide I′ bands, both of which report on the lipid-water interface. The shapes of both bands depend on lipid phase properties and are related to the ability of the lipids to form hydrogen bonds (15,26,27,37–39). We first focus on the hydrogen-bonded and nonhydrogen-bonded components of the amide I′ peak of POPC/SM at 18°C and 33°C (Fig. 6 *A*). The amplitude of the high-frequency component (nonhydrogen-bonded SM) increased significantly with changes in temperature, whereas the low-frequency component (hydrogen-bonded SM) changed its amplitude in the opposite direction. Additionally, both components remained at the same position. This suggests that POPC molecules have little influence on the hydrogen bonds between neighboring SM molecules in the transition region, again indicating the presence of unstable SM-rich domains. In contrast, when we compared the bands obtained at 33°C and 48°C (Fig. 6 *B*), we found that the two components shifted only their frequencies, and not their amplitudes, indicating ideal mixing outside the main phase transition regime in agreement with the above discussion of the CH_2 band.

Upon addition of Cer, ν_{CH2} decreased over most of the studied temperature intervals (Fig. S4), indicating that Cer stabilizes the gel phase, in agreement with our x-ray data. In similarity to POPC/SM, no sharp, edge-like changes were observed as a function of temperature, although the temperature behavior was more complex in the presence of Cer due to the proximity of the two transition regimes (Fig. 1). However, the smooth ν_{CH2} changes indicate the presence of phase fluctuations in POPC/SM/Cer mixtures. This notion is corroborated by an analysis of the amide I′ band (Fig. 7). Cer shifted the amide I′ band to lower wave numbers, suggesting increased hydrogen bonding and consequently a strong interaction between SM and Cer. Decomposition of the band into its individual components showed an additional third component at ~1615 cm^{-1} at

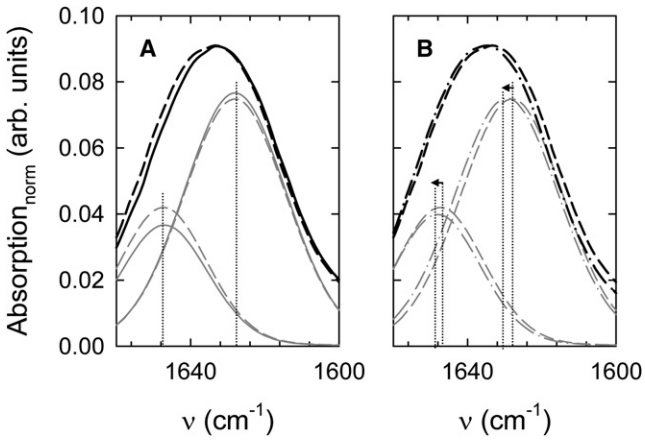

FIGURE 6 Zoom of the amide I′ band region for POPC/SM samples at 18°C and 33°C (*A*), and 33°C and 48°C (*B*). Black solid line: 18°C data; black dashed line: 33°C data; black dashed-dotted line: 48°C data. Gray lines show the corresponding estimates of nonhydrogen-bonded and hydrogen-bonded populations. Dotted vertical lines give the peak positions of subcomponents. Arrows in panel *B* indicate shifts to higher frequencies with increasing temperature. Absorption bands were normalized to the same amplitude. See also Fig. S5.

39°C for samples with >5 mol % Cer (i.e., just below T_{m2}; Fig. 7 *A*). The position of this component suggests the absorption of pure, hydrogen-bonded Cer (40) and thus points to the presence of a Cer-rich microscopic phase $L_\beta(u)$. Of interest, we were unable to discern this additional component above T_{off2} (Fig. 7 *B*), which indicates that Cer forms a more homogeneous mixture with SM above T_{m2}.

Finally, the behavior of the carbonyl band did not show any significant changes with temperature or Cer concentration (Fig. S7). This means that the properties of POPC at the water-lipid interface were not affected by the addition of Cer. We also compared the carbonyl band for pure POPC and POPC/SM mixtures and again found no significant difference (data not shown). This justifies our decomposition of the symmetric methylene band into pure POPC and pure SM components, as described above (Fig. 5, *B* and *C*).

Comparison with EPR data

To address the possible limitations of the labeling techniques used, we labeled the same samples with MeFASL (10,3) assuming uniform partitioning of the spin label into the coexisting domains based on previous data on phosphocholine/cholesterol mixtures (41). We observed a general agreement of EPR data with the expected temperature dependence of lipid ordering, i.e., the spectra at low temperatures were characteristic for gel phase and the spectra at high temperatures were characteristic for fluid phase (Fig. S8). However, the shape of EPR spectra showed only insignificant differences in the presence of Cer. This was particularly evident at 37°C, where our DSC, x-ray, and ATR-FTIR data all showed a coexistence of $L_\alpha(s)$ and $L_\beta(s)$ phases. This implies that the spin probe used here does not report efficiently on the presence of Cer, very likely because of insufficient partitioning into the Cer-rich gel domains. A multiprobe approach similar to that performed with fluorescence labels (23) would be needed to address this issue; however, such an approach was beyond the scope of this work. Nevertheless, our results demonstrate that one must take care when using a labeling technique.

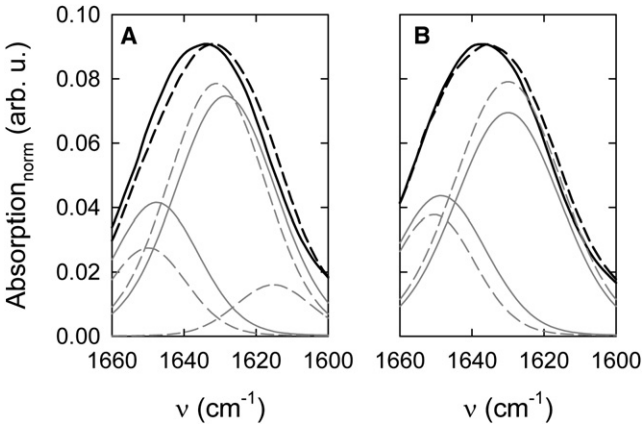

FIGURE 7 Comparison of the amide I′ band shape in the absence (*black solid lines*) and presence of 20 mol % Cer (*black dashed lines*) at 39°C (*A*) and 63°C (*B*). The gray lines show the corresponding estimates for the underlying components. In the presence of Cer, we found an additional low-frequency component corresponding to pure hydrogen-bonded Cer. This component cannot be distinguished at 63°C. Absorption bands were normalized to the same amplitude. See also Fig. S6.

Resultant phase diagram

We used the results from the x-ray, DSC, and IR experiments to construct a pseudobinary partial phase diagram (Fig. 8) along the SM + Cer = 50 mol % line of the complete ternary phase diagram. From our data, we were able to distinguish the regimes of microscopic and macroscopic phase separation, respectively. The borders are subject to uncertainties from the determination of T_{on}/T_{off} and the increment in Cer molar ratio.

Our measurements provide evidence for the presence of unstable, microscopic domains—$L_\alpha(u)$ and $L_\beta(u)$—in the POPC/SM equimolar mixture. This evidence is based in particular on the broad main transition range (Fig. 1) and the changes in IR band shapes and positions (Figs. 5 and 6, and Fig. S7), respectively, as well as the absence of stable domains in x-ray experiments (20).

For $0.05 \leq x_{Cer} \leq 0.3$, we observed a macroscopic coexistence of $L_\alpha(s)$ and $L_\beta(s)$ phases over a broad temperature range by x-ray experiments (Figs. 2 and 4) (20,22). The splitting of the main phase transition into T_{m1} and T_{m2} by

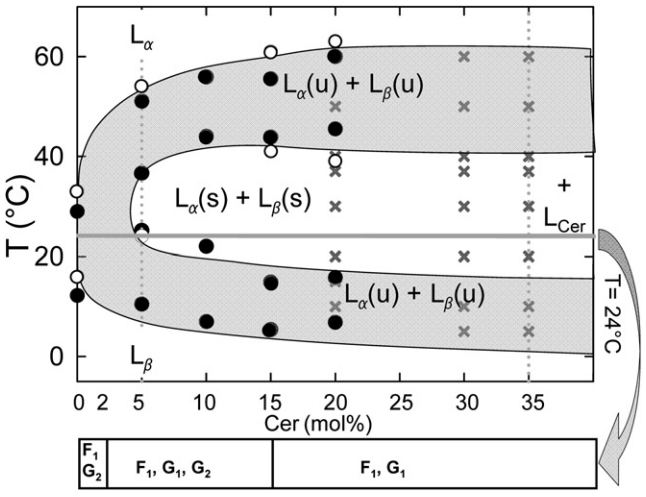

FIGURE 8 Pseudobinary partial phase diagram of fully hydrated POPC/SM/Cer mixtures along the SM + Cer = 50 mol % line of the complete ternary phase diagram. Solid circles: derived from DSC; open circles: derived from ATR-FTIR. Crosses correspond to the presence of a WAXS gel peak. Phase boundaries are drawn to guide the eye. The widths of the phase transitions regions were assumed to remain constant toward higher Cer concentrations. The horizontal line indicates the temperature cut studied by Castro et al. (23), where they observed the F_1, G_1, and G_2 phases.

Cer (Fig. 1) and the concomitant shifts to lower and higher temperatures with Cer content indicate that the L_α(s) phase is enriched in POPC, whereas the L_β(s) phase contains mainly SM and Cer. The preferred pairwise interaction between SM and Cer is most likely due to hydrogen bonding given by the N–H and C=O groups. The amide group can act as both proton donor and acceptor, whereas the carbonyl group is a proton acceptor (38). This leads to a depletion of SM from the L_α(s) as reported previously (20). Further support for this notion comes from our IR experiments, which showed increased hydrogen-bonding activity in the presence of Cer for the amide-I′ band (Fig. 7), whereas the carbonyl band, reflecting the properties at the POPC lipid-water interface, was affected only marginally (Fig. S7).

Of interest, the L_β(s) phase does not melt in a highly cooperative fashion. This is clearly shown by the width of the T_{m2} transition, which is approximately equal to that of T_{m1} (Table 1). Previous DSC experiments also revealed a broadening of the melting transition for SM/Cer mixtures (31), in agreement with our results. This appears to contrast with the high affinity between Cer and SM reported previously (20,23) and also supported by our data. However, our WAXS data show that the average correlation length of lipids in the L_β(s) phase is rather small (Fig. 3 *B*), i.e., on the order of several hundred angstroms. Thus, the cooperative unit for melting will be also small, resulting in a broad phase transition regime. Therefore, as the system approaches T_{m2}, it enters into a regime of phase fluctuations of L_α(u) and L_β(u) microscopic domains, which coexist with L_α(s) and L_β(s). Further, because of the melting properties of pure SM and Cer (30,32), L_α(u) will be enriched in this case in SM, and L_β(u) will contain predominantly Cer. In fact, we were able to discern microscopic Cer-rich domains by IR (Fig. 7 *A*).

It is instructive to discuss our results in comparison with the ternary phase diagram previously developed by Castro et al. (23) for POPC/SM/Cer. The only difference between their system and ours is that Castro et al. used C16:0-SM instead of egg-SM. They constructed their phase diagram at 24°C using mainly fluorescence spectroscopy and applying a multiple-probe technique. Along the SM + Cer = 50 mol % line, these authors observed the coexistence of a POPC-rich and SM-rich phase for Cer $\leq$ 2 mol %, denoted as F_1 and G_2. At higher Cer concentrations (up to Cer = 15 mol %), an additional Cer-rich phase (termed G_1) was observed. Finally, for Cer $>$ 15 mol %, they noted the coexistence of F_1 and G_1, but no longer observed the G_2 phase. No information on the stability of these phases was provided. The direct comparison with our results closes this gap.

In the absence of Cer, we observed the coexistence of unstable microscopic domains that were rich in either POPC or SM. Thus, F_1 and G_2 correspond to L_α(u) and L_β(u), respectively. In the presence of Cer, the microscopic domains became macroscopically stable and L_β(s) in particular was found to be enriched in Cer and SM. Thus, G_1 corresponds to the L_β(s) phase. Although our lowest Cer concentration was 2.5 times larger than that used by Castro et al. (23), we think that our findings will also apply to 2 mol % Cer. In the presence of Cer, the F_1 phase becomes stable and matches the L_α(s) phase. Further, if we consider the temperature axis of the phase diagram (Fig. 8), we can also understand the origin of the G_2 phase reported in this regime (23). In this Cer concentration range, the 24°C chosen by Castro and co-workers is very close to the T_{m1} phase transition regime. Considering the uncertainties in determining T_{on} and T_{off} in our study, and the fact that we used egg-SM instead of C16:0 SM, it is possible that their system was also in the phase transition regime, i.e., exhibiting compositional fluctuations. Thus, G_2 would also correspond to unstable microscopic domains L_β(u) in the presence of Cer, due to the vicinity of the phase transition. However, there is one problem with this comparison: we miss the L_{Cer} phase. Castro et al. did not differentiate between Cer domains dissolved in the lipid bilayers and Cer precipitates that we clearly observed above Cer $\geq$ 35 mol % (22) and were previously observed by transmission electron microscopy by Silva et al. (42). It is possible that Cer domains were present that remained undetected because the probes used by Castro et al. (23) do not incorporate easily into Cer crystals. Thus, their probes reported exclusively on Cer gel domains dissolved in the lipid bilayer. Aside from the fact that we used a different SM in our study, these discrepancies may also be due to the different approaches used in the two studies, i.e., fluorescence probe spectroscopy versus a label-free methodology.

CONCLUSIONS

In this work, we combined three label-free techniques to probe local and global, as well as fast and slow structural properties of POPC/SM/Cer mixtures. This allowed us to differentiate between unstable microscopic demixing and macroscopic stable domains, excluding putative influences on the phase behavior by labels. Additionally, we demonstrated possible problems in detecting domains when using a single label. The physics of lipid domains and their role in affecting membrane protein activity crucially depend on their stability and size. Therefore, these factors must be taken into account for any phase mapping of lipid mixtures. Additionally, this information can also help to reconcile discrepancies (33,43) that are mainly due to the experimental window of the applied technique. With our case study, we have demonstrated one possible way in which this can be achieved.

SUPPORTING MATERIAL

Eight figures and additional references are available at http://www.biophysj.org/biophysj/supplemental/S0006-3495(11)00323-7.

The ATR-FTIR spectroscopy experiments were conducted at the SISSI beamline (Sincrotrone Trieste) with technical support from Dr. Lisa Vaccari and Dr. Diane Eichert.

Z.A. received financial support from the Slovenian Research Agency (program No. P1-0060).

REFERENCES

1. van Meer, G., D. R. Voelker, and G. W. Feigenson. 2008. Membrane lipids: where they are and how they behave. *Nat. Rev. Mol. Cell Biol.* 9:112–124.
2. Escribá, P. V., J. M. González-Ros, …, G. Barceló-Coblijn. 2008. Membranes: a meeting point for lipids, proteins and therapies. *J. Cell. Mol. Med.* 12:829–875.
3. Lingwood, D., and K. Simons. 2010. Lipid rafts as a membrane-organizing principle. *Science.* 327:46–50.
4. Veatch, S. L., and S. L. Keller. 2005. Seeing spots: complex phase behavior in simple membranes. *Biochim. Biophys. Acta.* 1746:172–185.
5. Bagatolli, L. A. 2006. To see or not to see: lateral organization of biological membranes and fluorescence microscopy. *Biochim. Biophys. Acta.* 1758:1541–1556.
6. Feigenson, G. W. 2006. Phase behavior of lipid mixtures. *Nat. Chem. Biol.* 2:560–563.
7. Goñi, F. M., A. Alonso, …, J. L. Thewalt. 2008. Phase diagrams of lipid mixtures relevant to the study of membrane rafts. *Biochim. Biophys. Acta.* 1781:665–684.
8. Pabst, G., N. Kucerka, …, J. Katsaras. 2010. Applications of neutron and X-ray scattering to the study of biologically relevant model membranes. *Chem. Phys. Lipids.* 163:460–479.
9. Ayuyan, A. G., and F. S. Cohen. 2006. Lipid peroxides promote large rafts: effects of excitation of probes in fluorescence microscopy and electrochemical reactions during vesicle formation. *Biophys. J.* 91: 2172–2183.
10. Veatch, S. L., S. S. Leung, …, J. L. Thewalt. 2007. Fluorescent probes alter miscibility phase boundaries in ternary vesicles. *J. Phys. Chem. B.* 111:502–504.
11. Zhao, J., J. Wu, …, G. Feigenson. 2007. Phase studies of model biomembranes: macroscopic coexistence of Lα+Lβ, with light-induced coexistence of Lα+Lo phases. *Biochim. Biophys. Acta.* 1768:2777–2786.
12. Morales-Penningston, N. F., J. Wu, …, G. W. Feigenson. 2010. GUV preparation and imaging: minimizing artifacts. *Biochim. Biophys. Acta.* 1798:1324–1332.
13. Heimburg, T. 2007. Thermal Biophysics of Membranes. Wiley-VCH, Berlin.
14. Mendelsohn, R., and D. J. Moore. 1998. Vibrational spectroscopic studies of lipid domains in biomembranes and model systems. *Chem. Phys. Lipids.* 96:141–157.
15. Veiga, M. P., J. L. Arrondo, …, D. Marsh. 2001. Interaction of cholesterol with sphingomyelin in mixed membranes containing phosphatidylcholine, studied by spin-label ESR and IR spectroscopies. A possible stabilization of gel-phase sphingolipid domains by cholesterol. *Biochemistry.* 40:2614–2622.
16. Bloom, M., and J. L. Thewalt. 1995. Time and distance scales of membrane domain organization. *Mol. Membr. Biol.* 12:9–13.
17. van Blitterswijk, W. J., A. H. van der Luit, …, J. Borst. 2003. Ceramide: second messenger or modulator of membrane structure and dynamics? *Biochem. J.* 369:199–211.
18. Fruhwirth, G. O., and A. Hermetter. 2008. Mediation of apoptosis by oxidized phospholipids. *Subcell. Biochem.* 49:351–367.
19. Goñi, F. M., and A. Alonso. 2009. Effects of ceramide and other simple sphingolipids on membrane lateral structure. *Biochim. Biophys. Acta.* 1788:169–177.
20. Pabst, G., B. Boulgaropoulos, …, P. Laggner. 2009. Effect of ceramide on nonraft proteins. *J. Membr. Biol.* 231:125–132.
21. Gulbins, E., S. Dreschers, …, H. Grassmé. 2004. Ceramide, membrane rafts and infections. *J. Mol. Med.* 82:357–363.
22. Boulgaropoulos, B., H. Amenitsch, …, G. Pabst. 2010. Implication of sphingomyelin/ceramide molar ratio on the biological activity of sphingomyelinase. *Biophys. J.* 99:499–506.
23. Castro, B. M., R. F. de Almeida, …, M. Prieto. 2007. Formation of ceramide/sphingomyelin gel domains in the presence of an unsaturated phospholipid: a quantitative multiprobe approach. *Biophys. J.* 93: 1639–1650.
24. Garidel, P., C. Johann, and A. Blume. 2005. The calculation of heat capacity curves and phase diagrams based on regular solution theory. *J. Therm. Anal. Calorim.* 82:447–455.
25. Ohura, K., S. Kashino, and M. Haisa. 1972. The crystal and molecular structure of p-bromobenzoic acid. *Bull. Chem. Soc. Jpn.* 45:2651–2652.
26. Arsov, Z., and L. Quaroni. 2007. Direct interaction between cholesterol and phosphatidylcholines in hydrated membranes revealed by ATR-FTIR spectroscopy. *Chem. Phys. Lipids.* 150:35–48.
27. Arsov, Z., and L. Quaroni. 2008. Detection of lipid phase coexistence and lipid interactions in sphingomyelin/cholesterol membranes by ATR-FTIR spectroscopy. *Biochim. Biophys. Acta.* 1778:880–889.
28. Farkas, E. R., and W. W. Webb. 2010. Precise and millidegree stable temperature control for fluorescence imaging: application to phase transitions in lipid membranes. *Rev. Sci. Instrum.* 81:093704.
29. Pabst, G., A. Hodzic, …, P. Laggner. 2007. Rigidification of neutral lipid bilayers in the presence of salts. *Biophys. J.* 93:2688–2696.
30. Degovics, D., A. Latal, …, K. Lohner. 1997. Structure and thermotropic behaviour of mixed choline phospholipid model membranes. *J. Appl. Cryst.* 30:776–780.
31. Sot, J., L. A. Bagatolli, …, A. Alonso. 2006. Detergent-resistant, ceramide-enriched domains in sphingomyelin/ceramide bilayers. *Biophys. J.* 90:903–914.
32. Shah, J., J. M. Atienza, …, G. G. Shipley. 1995. Structural and thermotropic properties of synthetic C16:0 (palmitoyl) ceramide: effect of hydration. *J. Lipid Res.* 36:1936–1944.
33. de Almeida, R. F., A. Fedorov, and M. Prieto. 2003. Sphingomyelin/phosphatidylcholine/cholesterol phase diagram: boundaries and composition of lipid rafts. *Biophys. J.* 85:2406–2416.
34. Silva, L. C., R. F. de Almeida, …, M. Prieto. 2007. Ceramide-domain formation and collapse in lipid rafts: membrane reorganization by an apoptotic lipid. *Biophys. J.* 92:502–516.
35. Veatch, S. L., and S. L. Keller. 2005. Miscibility phase diagrams of giant vesicles containing sphingomyelin. *Phys. Rev. Lett.* 94:148101.
36. Busto, J. V., M. L. Fanani, …, A. Alonso. 2009. Coexistence of immiscible mixtures of palmitoylsphingomyelin and palmitoylceramide in monolayers and bilayers. *Biophys. J.* 97:2717–2726.
37. Mantsch, H. H., and R. N. McElhaney. 1991. Phospholipid phase transitions in model and biological membranes as studied by infrared spectroscopy. *Chem. Phys. Lipids.* 57:213–226.
38. Boggs, J. M. 1987. Lipid intermolecular hydrogen bonding: influence on structural organization and membrane function. *Biochim. Biophys. Acta.* 906:353–404.
39. Hubner, W., and A. Blume. 1998. Interactions at the lipid-water interface. *Chem. Phys. Lipids.* 96:99–123.
40. Moore, D. J., M. E. Rerek, and R. Mendelsohn. 1997. FTIR spectroscopy studies of the conformational order and phase behavior of ceramides. *J. Phys. Chem. B.* 101:8933–8940.
41. Arsov, Z., and J. Strancar. 2005. Determination of partition coefficient of spin probe between different lipid membrane phases. *J. Chem. Inf. Model.* 45:1662–1671.
42. Silva, L., R. F. M. de Almeida, …, M. Prieto. 2006. Ceramide-platform formation and -induced biophysical changes in a fluid phospholipid membrane. *Mol. Membr. Biol.* 23:137–148.
43. Veatch, S. L., K. Gawrisch, and S. L. Keller. 2006. Closed-loop miscibility gap and quantitative tie-lines in ternary membranes containing diphytanoyl PC. *Biophys. J.* 90:4428–4436.